JOURNAL OF GEOPHYSICAL RESEARCH: ATMOSPHERES, VOL. 118, 11,442–11,452, doi:10.1002/jgrd.50870, 2013

A global model of meteoric sodium

Daniel R. Marsh,[1] Diego Janches,[2] Wuhu Feng,[3] and John M. C. Plane[3]

Received 28 April 2013; revised 24 September 2013; accepted 27 September 2013; published 10 October 2013.

[1] A global model of sodium in the mesosphere and lower thermosphere has been developed within the framework of the National Center for Atmospheric Research's Whole Atmosphere Community Climate Model (WACCM). The standard fully interactive WACCM chemistry module has been augmented with a chemistry scheme that includes nine neutral and ionized sodium species. Meteoric ablation provides the source of sodium in the model and is represented as a combination of a meteoroid input function (MIF) and a parameterized ablation model. The MIF provides the seasonally and latitudinally varying meteoric flux which is modeled taking into consideration the astronomical origins of sporadic meteors and considers variations in particle entry angle, velocity, mass, and the differential ablation of the chemical constituents. WACCM simulations show large variations in the sodium constituents over time scales from days to months. Seasonality of sodium constituents is strongly affected by variations in the MIF and transport via the mean meridional wind. In particular, the summer to winter hemisphere flow leads to the highest sodium species concentrations and loss rates occurring over the winter pole. In the Northern Hemisphere, this winter maximum can be dramatically affected by stratospheric sudden warmings. Simulations of the January 2009 major warming event show that it caused a short-term decrease in the sodium column over the polar cap that was followed by a factor of 3 increase in the following weeks. Overall, the modeled distribution of atomic sodium in WACCM agrees well with both ground-based and satellite observations. Given the strong sensitivity of the sodium layer to dynamical motions, reproducing its variability provides a stringent test of global models and should help to constrain key atmospheric variables in this poorly sampled region of the atmosphere.

Citation: Marsh, D. R., D. Janches, W. Feng, and J. M. C. Plane (2013), A global model of meteoric sodium, *J. Geophys. Res. Atmos.*, *118*, 11,442–11,452, doi:10.1002/jgrd.50870.

1. Introduction

[2] The morphology of the mesospheric sodium (Na) layer that originates from the ablation of meteoroids is of interest for several reasons. First, it is readily observed from the ground using lidars and provides a way to measure the state of an atmospheric region that cannot easily be measured by in situ methods. Second, the Na layer has a relatively long chemical lifetime [*Xu and Smith*, 2003], is advected and diffused, and therefore can be used as a tracer in the study of the dynamics of the mesosphere and lower thermosphere (MLT). Third, model studies indicate that the Na column abundances provide information on the total meteoroid mass input rate: a quantity unknown to within a factor of at least 10 [*Plane*, 2012]. Fourth, the Na layer interacts with the neutral and ion chemistry and therefore tests our understanding of the chemistry and energetics of the MLT. Finally, recondensation of vaporized meteoric Na into "smoke" particles is thought to be a source of condensation nuclei for noctilucent clouds (NLC) [*Plane*, 2000]. An advantage of studying Na in the MLT is that it is observable both by ground-based instrumentation [e.g., *States and Gardner*, 1999; *Gardner et al.*, 2005; *Zhou et al.*, 2005; *Xu et al.*, 2006; *Yi et al.*, 2009; *Yuan et al.*, 2012] and from satellites [e.g., *Gumbel et al.*, 2007; *Fan et al.*, 2007; *Fussen et al.*, 2010]. This provides a great opportunity to validate the model dynamics and chemistry in an otherwise relatively poorly sampled region of the atmosphere.

[3] To date, there have been few studies that have attempted to quantitatively assess the consistency between meteoroid mass input rates, their geographical and seasonal variability, and measurements of mesospheric Na density, and we know of no study that attempts to do this within a fully consistent three-dimensional chemical-dynamical model. For example, in the previous one- and two-dimensional modeling studies by *Plane* [2004] and *Xu and Smith* [2003, 2004] the ionized background atmosphere is specified from International Reference Ionosphere [*Bilitza*, 2003] and not calculated self-consistently with the other

[1]National Center for Atmospheric Research, Boulder, Colorado, USA.
[2]Space Weather Lab, GSFC/NASA, Greenbelt, Maryland, USA.
[3]School of Chemistry, University of Leeds, Leeds, UK.

Corresponding author: D. R. Marsh, Atmospheric Chemistry Division, National Center for Atmospheric Research, PO Box 3000, Boulder, CO 80307-3000, USA. (email: marsh@ucar.edu)

2169-897X/13/10.1002/jgrd.50870

model constituents. This is important since the same dynamical motions (both resolved and subgrid scale) that affect Na directly via transport will also affect it indirectly via perturbations in reaction rates caused by changes in temperature, total density, and neutral and ion mixing ratios. In the study by *Gardner et al.* [2005] of metal layers at the South Pole, they were unable to reproduce the observed seasonal cycle in a one-dimensional model without increasing the input of metals by a factor of 1.7 during the months of May to August. They concluded that this additional source of metals most likely came from lower latitudes, transported by the mean meridional wind. More recently, lidar observations of winds, temperature, and sodium density have revealed that they all respond to planetary wave-driven variability originating in the lower stratosphere [*Yuan et al.*, 2012].

[4] This paper describes a new global model of Na species in the MLT that allows investigation of the effects of global-scale atmospheric motions including the mean meridional circulation, planetary waves, and atmospheric tides. The model is based on inclusion of interactive Na species chemistry and a realistic meteoritic Na source within a chemistry-climate model, both of which are described in the next section. Subsequent sections show the seasonal and short-term variability of Na species and compare them to a new, near-global, Na climatology based on observations. We also present comparisons with a number of published single-point observations. Overall, we find good agreement with observations and show that transport by the mean circulation does play a significant role in determining the seasonal cycle at high latitudes, as suggested by *Gardner et al.* [2005]. Our simulations indicate that temperature-dependent reaction rates and their effects on partitioning between the Na species play a secondary role compared to transport processes in determining the seasonal cycle.

2. Model Description

2.1. Whole Atmosphere Community Climate Model

[5] We utilize version 4 of the Whole Atmosphere Community Climate Model (WACCM), an extension of the Community Atmosphere Model (CAM) [*Neale et al.*, 2013]. WACCM is a "high-top" coupled chemistry model that has an upper boundary at 5.1×10^{-6} hPa (approximately 140 km). The free-running model has been used coupled to interactive ocean and sea ice model components in the Coupled Model Intercomparison Project phase 5 [*Marsh et al.*, 2013; *Calvo et al.*, 2012]. *Marsh et al.* [2013, and references therein] describe the extensions to the model physics necessitated by including the MLT. In this study, the model horizontal winds and temperatures in the troposphere and stratosphere are constrained by reanalysis, as was done by *Marsh* [2011]. Comparisons of modeled upper atmosphere winds and temperatures with available climatologies are presented by *Marsh* [2011], *Smith* [2012], and *Feng et al.* [2013]. Running the model constrained in this way enables comparison of model predictions to observed variations over a specific period. For example, the model is able to reproduce the effects in the mesosphere of the major stratospheric sudden warming (SSW) that occurred in early 2006 [*Marsh*, 2011]. The reanalyses used in this study are NASA's Modern-Era Retrospective Analysis for Research and Applications (MERRA) [*Rienecker et al.*, 2011]. Relaxation of the model dynamical fields to those of MERRA occurs from the surface to 40 km with a time scale of approximately 10 h. Between 40 and 50 km the amount of relaxation is linearly reduced such that at 50 km the model is free-running. The model has 88 levels and an approximate vertical resolution of two grid points per scale height in the MLT. Model horizontal resolution is 1.9° in latitude by 2.5° in longitude.

[6] As in the simulations by *Marsh et al.* [2013], daily solar spectral irradiances used in the calculation of photolysis and shortwave heating rates are specified from the model of *Lean et al.* [2005] and have been adjusted to reflect the new estimate of the total solar irradiance of *Kopp and Lean* [2011]. The chemistry scheme is based on that of *Kinnison et al.* [2007], which has 59 species and 217 gas-phase chemical reactions. It includes *E* region ion chemistry that solves for O^+, O_2^+, N^+, N_2^+, NO^+, and electrons. Ionization occurs from particle precipitation in the auroral regions and EUV and soft X-ray photons fluxes as described by *Marsh et al.* [2007] and varies daily based on the observed *Kp* planetary geomagnetic index and the 10.7 cm solar radio flux. The model does not include modification of the ionosphere by energetic solar protons but does include the production of hydrogen and nitrogen species that would result [see, e.g., *Jackman et al.*, 2009]. The chemistry scheme is augmented with the sodium chemistry scheme listed in *Plane* [2004, Table 1], which includes nine sodium species (Na, NaO, NaO_2, NaOH, $NaHCO_3$, Na^+, $NaCO_2^+$, NaH_2O^+, and NaN_2^+) and 26 gas-phase chemical and 5 photolysis reactions. However, unlike in the model of *Plane* [2004], no assumptions are made as to whether a constituent is in photochemical equilibrium, and all species are transported. Removal of Na species from the model is via dimerization of $NaHCO_3$, where the resulting dimer is not retained in the model:

$$2NaHCO_3 + M \rightarrow (NaHCO_3)_2 + M. \quad (1)$$

[7] The calculated rate coefficient for the dimerization of $NaHCO_3$ is $8.8 \times 10^{-10}(T/200\,K)^{-0.23}$ cm^3 molecule^{-1} s^{-1}, estimated from the dipole-dipole capture rate [*Plane*, 2004]. However, $NaHCO_3$ can also polymerize with other meteoric constituent molecules, in particular FeOH. Since the relative ablation rate of Fe:Na is about 4:1 [*Gardner et al.*, 2005; *Feng et al.*, 2013], we increase the rate coefficient of (1) by a factor of 5. As in the recent companion paper by *Feng et al.* [2013], which describes mesospheric Fe chemistry in WACCM, uptake on meteoric smoke particles is treated as being equivalent to this dimerization reaction as was shown by *Plane* [2004]. A future version of the model with multiple meteoric metals will explicitly model the formation of meteoric dust particles from the polymerization of metal compounds and the uptake of sodium on those particles.

2.2. Meteoroid Input Function

[8] The meteoroid input function (MIF) specifies the temporal and geographical input of meteoritic metallic atoms in the MLT and is based on calculations from two recently developed models. The first model uses current knowledge of the astronomical characteristics of the sporadic meteor complex to estimate the global meteoric mass flux into the Earth's upper atmosphere. A detailed description of this is presented by *Janches et al.* [2006], *Fentzke and Janches* [2008], and *Fentzke et al.* [2009].

The model estimates the meteoric mass which is deposited at each altitude within the MLT at all latitudes for each day of the year. It calculates the contribution from particles in the size range of 10^{-15} to 10^{-6} kg, which make up the bulk of metallic input into the upper atmosphere [*Ceplecha et al.*, 1998]. Particles larger than 10^{-6} kg are relatively infrequent, and particles smaller than 10^{-15} kg will decelerate without ever reaching the high temperatures (> 1800 K) required to significantly ablate.

[9] It is assumed that all meteoritic input originates from six main sporadic meteoroid populations, and we assign their characteristics (i.e., velocity, diurnal variability, and entry angle) accordingly, utilizing as a starting point the flux curves presented in *Ceplecha et al.* [1998]. Specifically 33% of the meteors are assigned to the apex, 22% to the helion, 22% to the antihelion, 11.5% to the north toroidal, and 11.5% to the south toroidal. This enables calculation of the time evolution of the population's incoming angular and velocity characteristics in a given geographical location. The model has been validated against High Power and Large Aperture radar head echo observations [*Janches et al.*, 2006; *Fentzke and Janches*, 2008; *Fentzke et al.*, 2009; *Pifko et al.*, 2013]. Unlike those studies, however, we consider all particles large and fast enough to ablate, without considering if the amount of electrons produced during entry is large enough for detection by a sensitive radar [*Janches et al.*, 2008]. The result is the distribution of particles as a function of time, initial mass, initial absolute velocity, and entry angle calculated with a resolution of 1 min, 10 divisions per decade in $\log_{10}$(mass), 1 km s^{-1}, and 1°, respectively. This calculation is performed for every day of the year and from pole to pole every 5° in latitude. The average velocity of particles from the apex, helion, and antihelion populations is around 30 km s^{-1}, which comprises 77% of particles. Both toroidal populations have mean velocities of approximately 55 km s^{-1}.

[10] Once this flux is estimated, we utilize a second model, the Chemical Ablation Model (CABMOD) developed by *Vondrak et al.* [2008], to calculate the ablation and ionization of the individual chemical elements in the meteoroid. CABMOD is capable of calculating the quantity of ablated atoms along the meteoroid path as each species is differentially deposited in the MLT. The more volatile elements (Na and K) are released first when the temperature is still relatively low. As the meteoroid penetrates deeper into the atmosphere and the atmospheric density increases, the particle collides with a sufficient number of air molecules to raise its temperature to the point (∼1800 K) where the main chemical constituents (Si, Fe, and Mg) evaporate. This will occur ∼12 km lower than where the alkalis were evaporated first. Finally, the ablation of the most refractory meteoroid constituents (mostly Ca, Ti, and Al) will occur only if the particle's kinetic energy is sufficient to raise its temperature beyond ∼2500 K [*Vondrak et al.*, 2008; *Janches et al.*, 2009]. CABMOD was used to generate look-up tables (LUT) containing the ablation profiles of each metallic element as a function of meteoroid mass, velocity, and entry angle. The respective resolutions of the LUT were 10 divisions per decade of mass, 5 km s^{-1}, and 5°. Interpolation was then used to determine the ablation profile for each individual meteoroid resulting from the astronomical model.

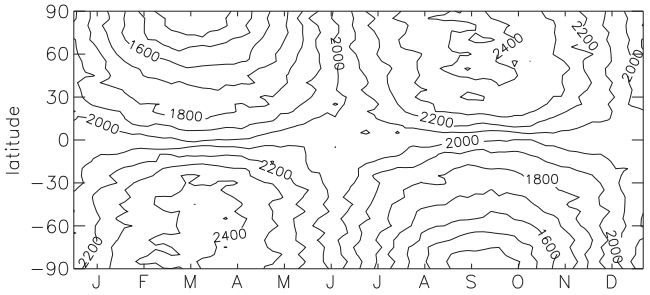

Figure 1. Seasonal and latitudinal distribution of meteoric Na column injection rates (atoms cm^{-2} s^{-1}) used in the WACCM simulation.

[11] Finally, we integrate the ablation profiles over the distribution of incoming particles to obtain a Na input profile as a function of day of the year, latitude, and height. The annual cycle of the column integral of the Na input used in WACCM simulations is shown in Figure 1. The same cycle is used for every year of simulation. In the extratropics the cycle is annual, peaking in September in the Northern Hemisphere (NH) and March in the Southern Hemisphere (SH) with input rates in excess of 2400 atoms cm^{-2} s^{-1}. The amplitude of the cycle is largest near the poles, where it reaches about 28% of the annual mean. In the tropics the MIF is relatively constant at around 2000 atoms cm^{-2} s^{-1}. The annual and global mean input of sodium is 1.75×10^8 atoms cm^{-2} d^{-1}. Integrated over the globe, the sodium mass input is 0.035 t d^{-1}. Assuming a relative elemental abundance of 0.8% [*Vondrak et al.*, 2008], the total ablated meteoritic mass input would be equivalent to 4.6 t d^{-1}. We note that this is at the low end of the range of the estimates of the total (ablated and non-ablated) daily input of cosmic dust input which extends to nearly 300 t d^{-1} [*Plane*, 2012]. Possible changes to the model that could permit a higher mass input are considered in section 5 and by *Feng et al.* [2013].

3. Results: Global Distribution and Seasonal Variations

[12] For this study we simulated the period 2004 to 2009. The first year is not included in analysis to exclude any model start-up transients. Figure 2 shows the WACCM global mean density altitude profiles for the calculated Na-bearing species averaged for the month of July. At altitudes above approximately 93 km, Na^+ is dominant, although it is still a relatively minor positive ion, being at most around a percent of all ions. Below that neutral atomic Na has the largest density down to approximately 80 km, below which $NaHCO_3$ is the largest. NaO_2 reaches a maximum of 15% of the total near 80 km. The combination of these four species accounts for 97% of all Na-bearing species between 70 and 110 km. We calculate that Na species reach a peak global mean concentration of around 3400 cm^{-3} at approximately 92 km. The profiles calculated are in qualitative agreement with previous model estimates [e.g., *Plane*, 2004; *Xu and Smith*, 2003] in that the relative location of each layer is the same.

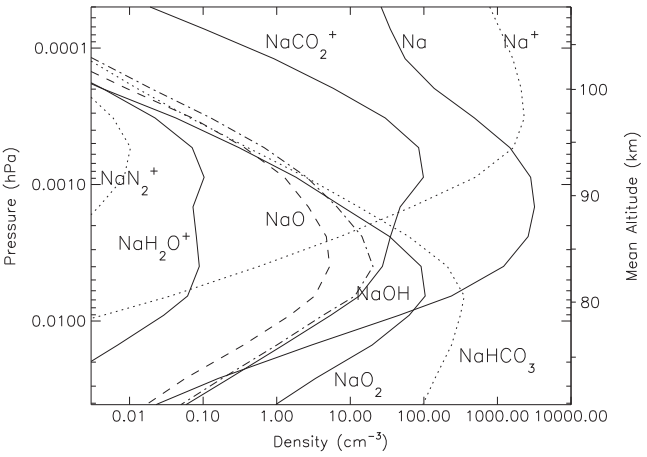

Figure 2. Global mean distribution of sodium compounds during July.

[13] In Figure 3 the latitudinal and seasonal variations of the monthly mean column integrals of Na^+, Na, and $NaHCO_3$ are shown. Extratropical Na^+ peaks in late summer and of the three species resembles the MIF variations the most. In contrast, extratropical Na and $NaHCO_3$ have maxima in winter. The largest Na column densities are seen in the high-latitude Southern Hemisphere during June and July, where the total column exceeds 9×10^9 atom cm^{-2}. In the tropics Na^+ and $NaHCO_3$ are relatively constant, whereas Na has a semiannual variation with maximum values during equinox. Inspection of the sum of the three species (Figure 3d) reveals that the drastically different seasonal variations cannot simply be caused by a chemical repartitioning of the available meteoritic Na species family, since the sum would then also follow the MIF. Instead, the model predicts that the largest total column values occur over the SH winter pole, again indicating that convergence of the Na flux over the poles plays a role.

[14] Figure 4 shows the ratio of Na^+ to Na calculated from the monthly means shown in Figure 3. The ratio ranges from below 0.4 to above 3. Averaged over all seasons and latitudes, the ratio is close to unity. This is larger than the ratio determined from rocket-borne mass spectrometric Na^+ measurements of between 0.2 and 0.25 by *Plane* [2004]. However, that estimate is based on just five rocket flights [*Kopp*, 1997] that did not simultaneously measure Na and do not represent an annual and global average (all flights lie between 37 and 68°N). Also, the rocket profiles reported by *Kopp* [1997] show very large variability in their vertical structure, as might be expected from a single-point measurement. Still, if we average the modeled ratio at the latitude and month of the rocket flights, we obtain a ratio 0.9, which, while on the lower end of the modeled range of ratios, is larger than derived from observations. A similar discrepancy was reported by *Plane* [2004], who states that the modeled ratio could be reduced by reducing the average entry velocity of incoming meteors such that they ablate lower in the atmosphere. Work is ongoing to evaluate if such a reduction is compatible with the astronomical model of meteor fluxes described in section 2.2.

[15] The seasonal variation of the altitude of the peak of the Na layer is shown in Figure 5. The altitude was calculated by finding the geometric height of the maximum of a quadratic polynomial fit to the sodium density at the three levels that span the peak sodium density. In choosing three points, the fit is unique and easily differentiated to find the height of the maximum. At middle to high latitudes the seasonal cycle is predominantly annual, with the peak of the layer occurring at a higher altitude during summertime, likely caused by upwelling over the summer pole. In the

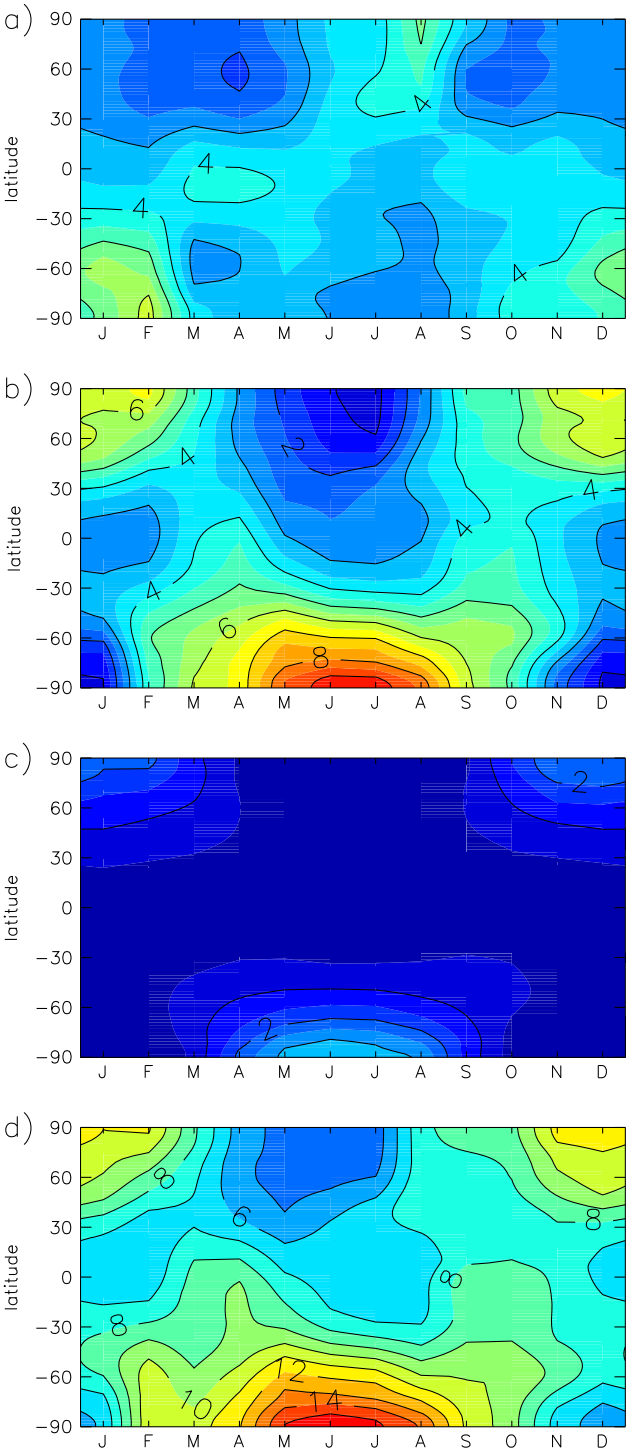

Figure 3. Monthly mean total column (10^9 cm^{-2}) of (a) Na^+, (b) Na, (c) $NaHCO_3$, and (d) their sum.

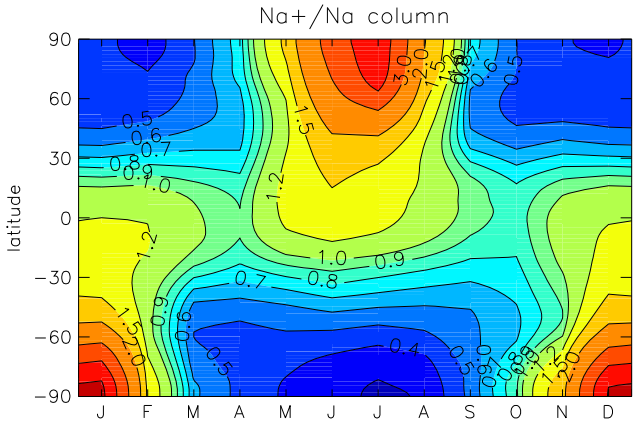

Figure 4. Ratio of Na^+ to Na monthly mean column shown in Figures 3a and 3b. Contour levels are [0.3, 0.4, 0.5, 0.6, 0.7, 0.8, 0.9, 1, 1.2, 1.5, 2, 3, 4, 5].

tropics, there is a semiannual oscillation in the layer peak height, with minima in April and September/October. The annual mean value varies with latitude between 89.8 and 87.5 km, with the tropics higher than the high latitudes. The global annual mean layer peak height is 89.1 km.

[16] Figure 6 shows the latitude and time variation of zonal mean column sodium from years 2006 to 2009. Differences between years are the result of internally generated variability, variations in external forcing (e.g., solar variability), and the MERRA reanalysis. Overall, it appears that the seasonal cycle is consistent from year to year. There does appear to be a large amount of day-to-day variability over the winter poles. In particular there is the very large increase above 60°N in February of 2009. This is preceded by lower column abundances in late January. To better visualize this rapid change, Figure 7 shows the NH polar cap on 22 January and 6 February 2009. On 22 January the column abundance is below 6×10^9 atom cm^{-2} almost everywhere. In contrast, on 6 February they exceed 10^{10} atom cm^{-2} over most of the pole northward of 60°N and can reach 2×10^{10} atom cm^{-2} above 80°N. The almost quadrupling of the Na column in 2 weeks is most likely associated with the major stratospheric sudden warming (SSW) that occurred on 24 January 2009 [*Butler and Polvani*, 2011; *Yuan et al.*, 2012].

[17] To illustrate this further, the NH polar cap temperature variations in the stratosphere and lower thermosphere during the first 100 days of 2008 and 2009 are shown in Figure 8. Between day 12 and day 23 of 2009, temperatures at 6.9 hPa increased by over 60 K, and at 0.002 hPa there was a major cooling. Over the following 40 days the stratospheric temperature slowly returned to its prewarming level. In the lower thermosphere, temperatures rebounded much more quickly and exceeded the prewarming values by almost 20 K. Temperatures stayed elevated in the lower thermosphere for several weeks following the rebound. In contrast, 2008 temperature variations were more sporadic, with many short-lived temperature swings. As discussed by *Marsh* [2011], the dramatic cooling and later heating in the lower thermosphere modeled in WACCM is caused by adiabatic heating from anomalous vertical motions over the pole. The changes in the vertical wind are the result of changes in the mean meridional wind, which in turn is caused by changes in gravity wave momentum deposition. Gravity wave propagation through the lower atmosphere is modified as the stratospheric mean winds change during the major warming. The result is that during the SSW the mean meridional wind reverses direction and flows away from the pole and leads to anomalous upwelling and cooling. Following the SSW, the wind returns to the normal poleward and downward flow, but it is stronger than prior to the SSW, and hence a strong mesospheric warming is simulated.

[18] One possible driver for the increase of Na by a factor of 3 (shown in Figure 8c) following the SSW then is via the effects of temperature changes in reaction rates. For example, the temperature dependence of neutral Na chemistry is mostly governed by the following reaction [*Plane*, 2004]:

$$NaHCO_3 + H \rightarrow Na + H_2 + CO_2, \quad k = 1.8 \times 10^{-13} T^{0.777} \exp(-1014/T). \tag{2}$$

[19] An increase of temperature would have the effect of increasing the net conversion of $NaHCO_3$ to Na. Increased downwelling of atomic H might also be important in converting $NaHCO_3$ to Na. However, conversion of the major reservoir species $NaHCO_3$ to Na is unlikely to explain the sudden rise, since this species increases following the SSW (see, e.g., Figure 8c). We note that Na^+ shows a similar temporal variation to $NaHCO_3$ and also increases following the SSW (not shown).

[20] Since a repartitioning of available Na species within the polar cap is therefore unlikely to explain the rapid decrease and increase, it leaves transport in and out of the cap as the cause. The upwelling and equatorward flow during the SSW would bring air poor in Na from lower altitudes and distribute this over the polar cap. Then, following the SSW, the enhanced downward and poleward flow would tend to transport Na species from midlatitudes into the polar region.

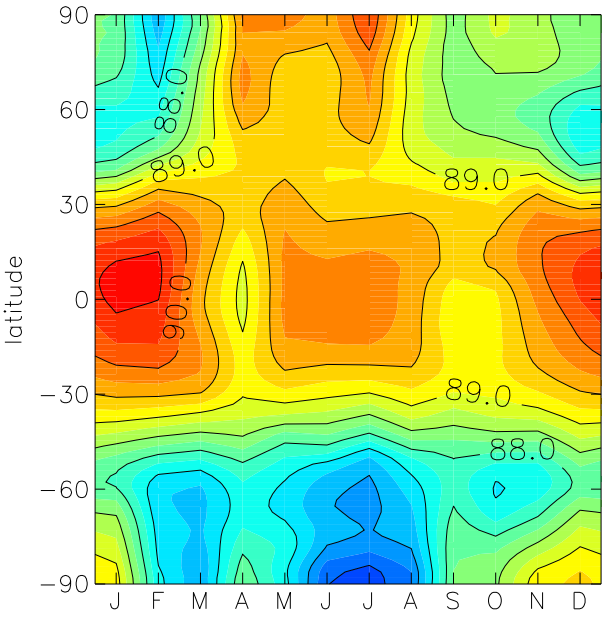

Figure 5. Sodium layer peak height (km). Contours are every 0.5 km.

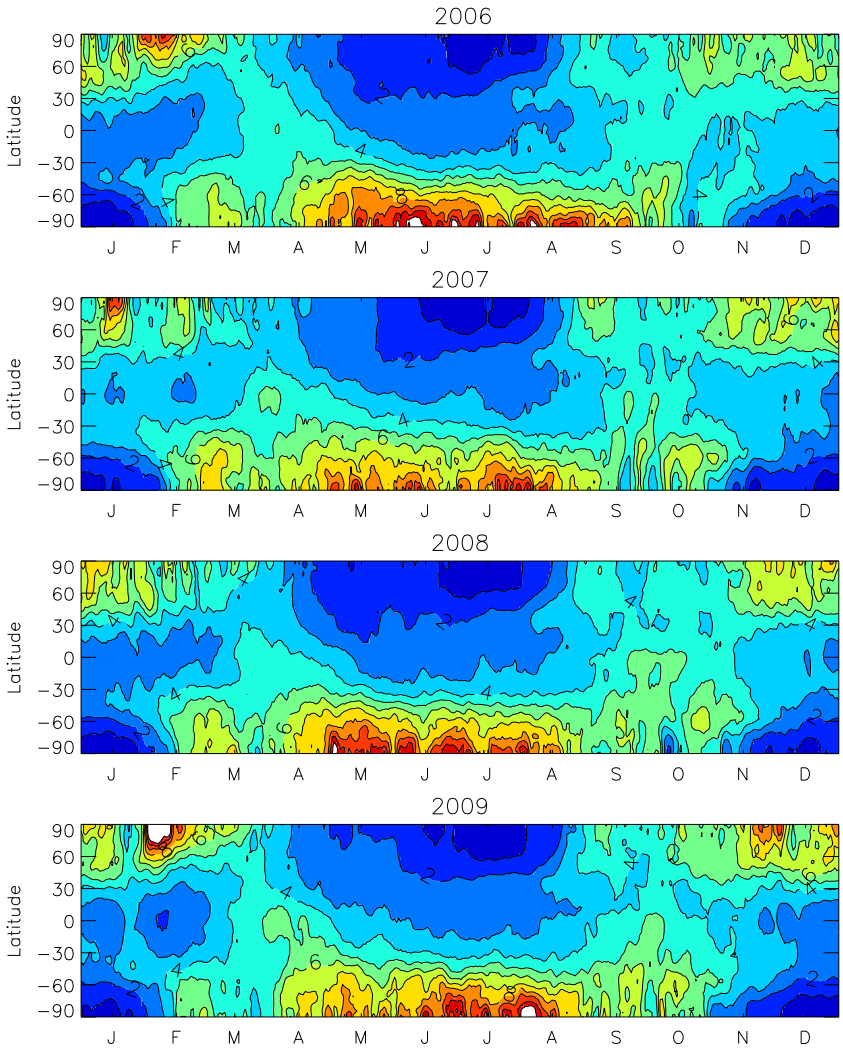

Figure 6. Zonal mean total column Na from years 2006 and 2009. Contours are every 10^9 cm^{-2}. Data smoothed in time with a 3 day running mean.

This is clearly seen in Figure 8d), which shows the column-integrated flux of Na species across the 70°N latitude circle divided by the area of the polar cap. We find that following the SSW the flux into the cap would be sufficient to increase the average column of Na species by almost 3×10^9 cm^{-2} per day. The poleward and downward flow would not only increase all Na species but also promote conversion of Na^+ to Na due to enhanced recombination rates as the density increases with downward motion. A similar mechanism is likely the cause of the low Na^+ to Na ratios seen in Figure 4 over the wintertime pole.

4. Comparison With Observations

4.1. A Na Reference Atmosphere

[21] In order to compare the WACCM model results with observations, we first constructed a reference atmosphere. This consists of zonally averaged data in 10° latitude bins on a monthly time scale. The reference atmosphere draws on several sources. The most comprehensive is the recent near-global set of satellite limb-scanning measurements made with the Optical Spectrograph and Infra-Red Imager System (OSIRIS) spectrometer on the Odin satellite [*Fan et al.*, 2007]. Because the data are self-consistent and ground-truthed against lidar observations [*Gumbel et al.*, 2007], it forms the backbone of the reference atmosphere. However, there are some limitations. First, the data cover only two complete years, 2003 and 2004. Second, the sun-synchronous orbit of Odin provided measurements only at about 0600 and 1800 local time. Since the Na layer is subject to photochemical and tidally driven diurnal variations [*Clemesha et al.*, 1982; *Fan et al.*, 2007], the data from both local times have been averaged. Third, OSIRIS measures Na resonance fluorescence in the dayglow, so measurements are restricted to periods when the mesosphere is illuminated (solar zenith angle <92°), and so there are no data at midlatitudes to high latitudes during winter. In order to partly overcome these limitations, lidar data from the South Pole for the years 1995–1997 [*Gardner et al.*, 2005], from São José dos Campos (23°S) for the years 1972–1986 [*Clemesha et al.*, 2004], and Urbana-Champaign (40°N) and Fort Collins (41°N) for the years 1991–1999 [*Plane et al.*, 1999; *States and Gardner*, 1999; *She et al.*, 2000] have been included. Lidar data from other observatories are either

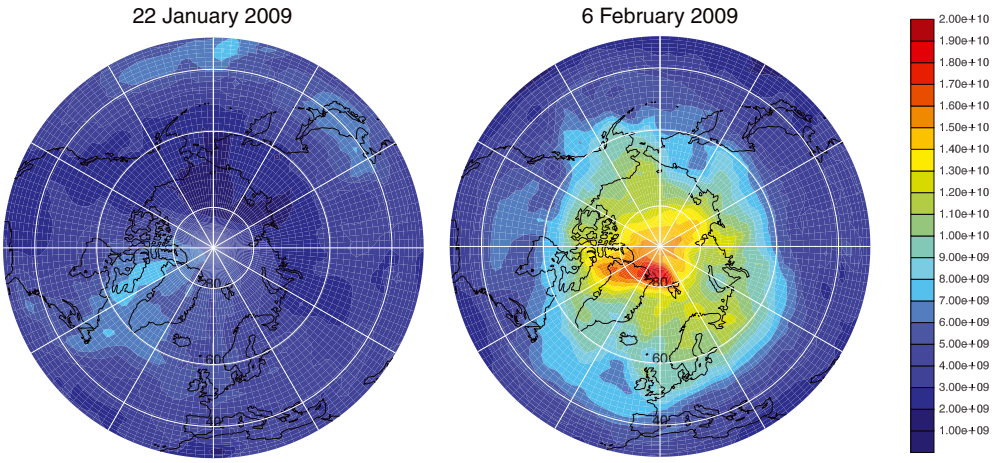

Figure 7. WACCM total column Na (cm^{-2}) at 00 UT on 22 January and 6 February 2009.

already covered by the satellite measurements or have not yet been published as a long-term record. It should be noted that the uncertainty in the absolute Na density near the layer peak retrieved from OSIRIS is ±10% [*Gumbel et al.*, 2007], similar to modern ground-based lidars. However, the natural variability of the Na layer means that the average monthly column abundance and peak density values in some of the 10° latitude bins have a larger uncertainty (up to ±30%), depending on the number of profiles in the average [*Fan et al.*, 2007]. The global map of Na column abundance was constructed starting from the satellite measurements in *Fan et al.* [2007, Figure 1]. This is a grid map of zonal monthly averages in 10° latitude bins. Available monthly averaged lidar data (see above) were then added to grid boxes where there were no OSIRIS data. The remaining empty grid boxes were then filled in by interpolation. The largest uncertainty in this exercise is the region between 30 and 80 °S, between April and August, where there are no measurements available. The Na column abundance at high northern latitudes in winter is consistent with the short lidar record published by *Tilgner and von Zahn* [1988].

[22] Although these data sets are taken from different decades and phases of the solar cycle, a long-term study of the Na layer [*Clemesha et al.*, 2004] shows that, at least at low latitudes (23°S), the effects of changing climate and the solar cycle on the Na layer are small. The centroid of the layer moves down only 0.17 ± 0.11 km between solar minimum and maximum. This downward trend is likely due

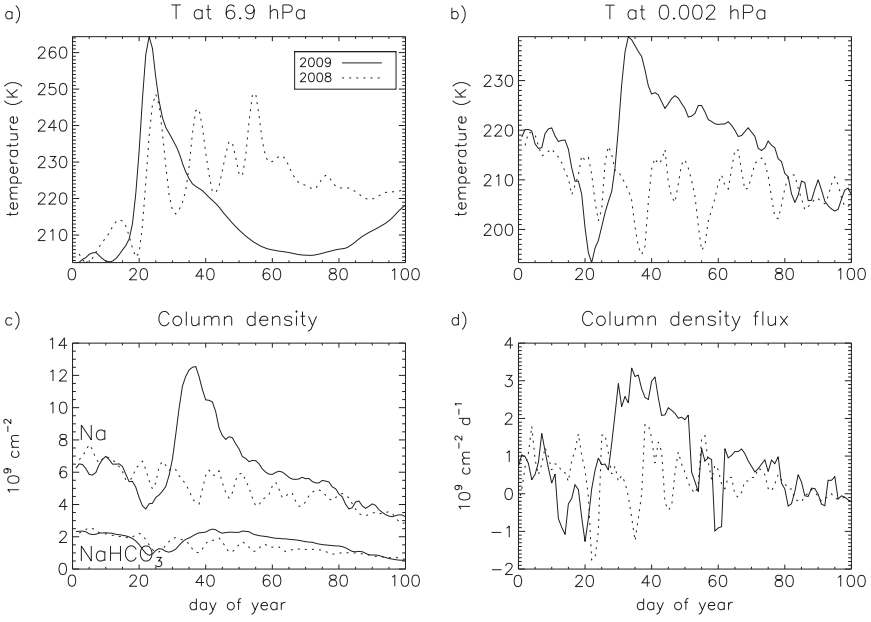

Figure 8. NH polar cap (> 70°N) average temperature at (a) 6.9 hPa and (b) 0.002 hPa during the first 100 days of 2008 (dotted lines) and 2009 (solid lines). (c) Na (upper curves) and $NaHCO_3$ (lower curves) total column (10^9 cm^{-2}) for the same time interval and location. (d) Flux of Na species through 70°N latitude circle divided by the area within the polar cap (10^9 cm^{-2} d^{-1}). All data have been smoothed in time with a 3 day running mean.

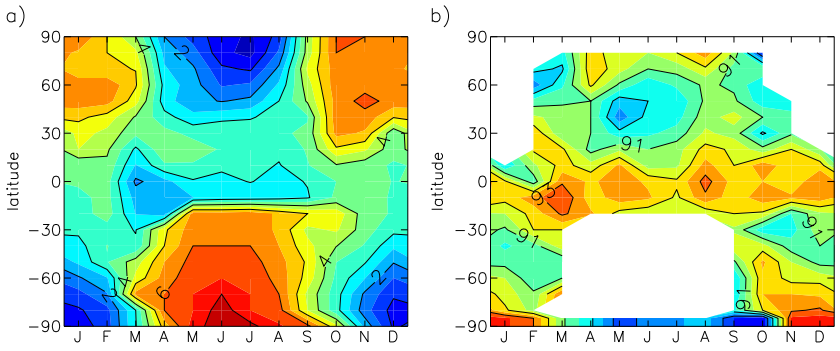

Figure 9. (a) Observed monthly mean total Na column (10^9 cm^{-2}) and (b) Na layer height (km).

to changes in chemistry: at solar maximum there is a greater plasma density in the lower *E* region and so more Na is converted to Na^+ on the topside, whereas higher atomic H and O concentrations below 90 km (produced by increased Lyman-α radiation) recycle Na from $NaHCO_3$ and other reservoir species more rapidly on the underside of the layer. Measurements made at Urbana-Champaign, Illinois (40°N) in 1991–1994 [*Plane et al.*, 1999] and 1996–1998 [*States and Gardner*, 1999], which correspond to periods at and shortly after solar maximum and minimum, respectively, show that the Na column abundance was about 20% higher at solar maximum.

[23] The resulting Na column abundance, as a function of latitude and month, is shown in Figure 9a. The average column abundance is 3.9×10^9 atom cm^{-2}, although this ranges by a factor of 20 ($0.33–7.4 \times 10^9$ atom cm^{-2}), depending on time and location. Abundances exhibit a seasonal variation very similar to WACCM with a wintertime maximum in the extratropics: October–November in the NH, and June–July in the SH. As in the model, the size of the variation is latitude dependent: at low latitudes the winter enhancement is only a factor of about 1.3, whereas at midlatitudes the wintertime enhancement is approximately a factor of 3 and more than 10 in the polar regions. In the tropics the variation is semiannual, peaking at equinox. The shift from an equatorial semiannual to polar annual cycle in both the observational climatology and WACCM confirms the finding of *Fussen et al.* [2010] based on observations from the Global Ozone Monitoring by Occultation of Stars (GOMOS) satellite.

[24] The agreement in the height of the layer (shown in Figure 9b) is not as good, with observed heights about 2–3 km higher than the model. The exact cause of this offset is difficult to assess, although it is within a model vertical grid spacing. The discrepancy may be related to errors in the background atmosphere density profile versus geometric altitude, which depends on the thermal structure. As noted by *Smith* [2012] the mesopause temperature in WACCM is warmer than satellite observations made by the Sounding the Atmosphere by Broadband Emission Radiometery instrument by over 10 K throughout the tropics and subtropics. However, the model does reproduce much of the observed latitudinal structure, with the layer being overall higher in the tropics and higher during summertime in the extratropics.

4.2. Lidar Comparisons

[25] The modeled and observed annual cycles of monthly mean column sodium at Fort Collins (41°N, 104°W) and the South Pole are shown in Figure 10. Both observational estimates are from lidar measurements: Fort Collins data are listed in *She et al.* [2000, Table 2], and the South Pole data are taken from the study by *Gardner et al.* [2005, Table 1]. Also shown are the zonal mean seasonal cycles from Figure 9a and the empirical fit to GOMOS measurements [*Fussen et al.*, 2010]. Both model and observations show a predominantly annual cycle, with minimum during the summer, consistent with Figure 3.

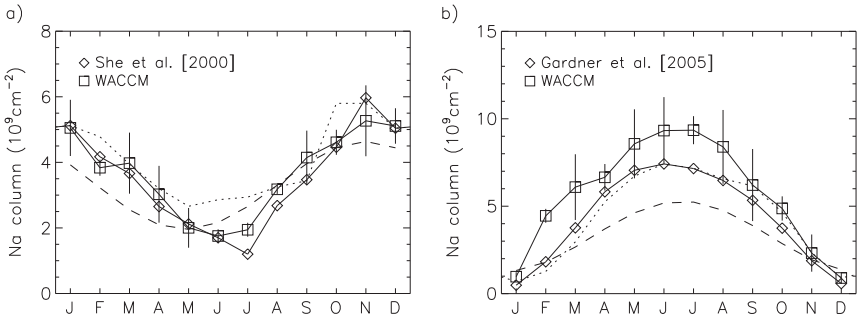

Figure 10. Observed and WACCM simulated column sodium (10^9 cm^{-2}) at (a) Fort Collins and (b) South Pole. WACCM data are monthly means calculated from years 2005 to 2009 (2σ estimate of the uncertainty in the model monthly mean shown as vertical bars). Dotted lines are climatological column estimates from Figure 9a. Dashed lines are from *Fussen et al.* [2010].

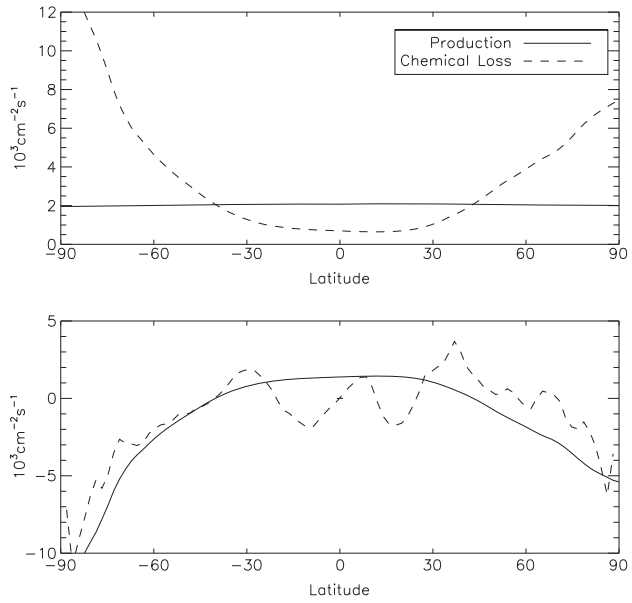

Figure 11. (a) Latitudinal distribution of the zonal mean Na species column-integrated meteoritic input (solid line) and chemical loss (dashed line) averaged over the years 2005 and 2008. (b) Production minus loss from Figure 11a (solid line) and divergence of the Na species meridional transport (dashed).

[26] The amplitude of the seasonal cycle is larger at the South Pole location compared to Fort Collins. WACCM is in better agreement with observations at Fort Collins than South Pole, with model values larger than observed during February, March, and July. The values from the GOMOS model are generally lower at the South Pole than the other estimates in seasons other than summer, but since GOMOS did not make observations at the South Pole during this time [*Fussen et al.*, 2010], the values there are likely an extrapolation from lower latitudes where the seasonal cycle is weaker. The summer minimum is significantly lower at the South Pole than at Fort Collins. A similar difference between observations at the South Pole and Urbana Atmospheric Observatory (40°N) was seen by *Gardner et al.* [2005]. They attributed the very low values at the South Pole to the uptake of sodium by NLC particles. Since this process is not included in these WACCM simulations, it appears that the very low sodium abundances that are seen in December and January are related more to the effects of dynamics. We note that removal of Na species via dimerization is a second-order reaction with a rate proportional to the square of the Na species density, whereas removal on NLC particles is proportional to the product of the Na species density and the NLC volumetric surface area, making dimerization more efficient where densities are large. The Na layer peak is at its highest altitude in summer, further distancing it from the maximum in the NLC volumetric surface area, which is around 87 km [*Plane et al.*, 2004]. Over the summer pole, densities of Na and $NaHCO_3$ at 87 km are around 10 and 1 cm^{-3}, respectively, so that even if uptake on NLC is very efficient it would not change the seasonal cycle of the column significantly. It should be noted that metals that have their maximum abundance lower in the atmosphere, such as Fe, will be more affected by NLC uptake, and this has been included in the model of *Feng et al.* [2013].

5. Discussion and Conclusions

[27] The relative importance of chemistry and transport in determining the seasonal cycle depends on the lifetimes for these processes. Considering all Na-bearing species, the MIF is the only source, and dimerization is the only loss. If the chemical lifetime (i.e., the inverse of the loss rate) is short compared to that of transport, then the distribution of Na species and their loss should look very much like the MIF. The latitudinal distribution, averaged over the years 2005 and 2008, of the column-integrated MIF and the zonal mean Na species removal via (1) are shown in Figure 11a. The MIF is relatively constant with respect to latitude, whereas the losses are greatly enhanced in the polar regions and lower than the meteoritic input at latitudes equatorward of 40°. Over the long-term, mass continuity dictates that the time average of differences between chemical production and loss ($\bar{S}$) are balanced by transport processes. Since Figure 11 shows annual and zonal averages of the column-integrated production and loss, that transport process must be related to net meridional transport. This can be expressed mathematically as follows:

$$\left\langle \frac{\partial \rho \bar{\chi}}{\partial t} \right\rangle = 0 = \langle \bar{S} \rangle - \left\langle \frac{1}{a \cos\phi} \frac{\partial}{\partial \phi} \left(\rho \bar{v}^* \bar{\chi} \cos\phi \right) \right\rangle, \qquad (3)$$

where $\bar{\chi}$ is zonal mean mixing ratio, ρ is density, ϕ is latitude, a is the radius of the Earth, and $\bar{v}^*$ is the transformed Eulerian mean meridional wind [*Smith et al.*, 2011]. Angle brackets denote the vertical integral over all altitudes. The last term on the right-hand side is the divergence of the Na species mean meridional transport (dashed line in Figure 11b). It is clear that much of the imbalance between production and loss is related to meridional transport. We see clearly that transport serves to move Na species away from the equator toward the poles where it is lost.

[28] Overall, the model appears to be capable of reproducing the seasonal and short-term variability of meteoric Na. This is achieved with a MIF model that has a total meteoric mass input of 4.6 t d^{-1}, mostly contributed by meteoroids with masses between 10^{-15} and 10^{-6} kg. Even though this amount is within the lower limit of estimates of this hotly debated quantity derived from a very diverse pool of observational techniques and measurements [*Plane*, 2012], it appears to be sufficient to model the global Na layer with very little or no scaling. We note, however, that there are several parameters in WACCM that could be adjusted to allow for a larger meteoric input, for example, the ad hoc increase in the dimerization of $NaHCO_3$ to account for the absence of other meteoritic metals. Future versions of the models will include additional metal species to better represent this loss process. Coupling WACCM to a sectional microphysics code that models the growth of meteoric dust such as described by *Bardeen et al.* [2008] would also permit uptake of metals on these particles.

[29] In addition, the eddy diffusion coefficient can be increased by decreasing the effective Prandtl number [*Smith et al.*, 2011], which would lead to downward transport of Na and quicker conversion to $NaHCO_3$. Sensitivity tests in WACCM with Fe chemistry show that halving the Prandtl

number (effectively doubling the eddy diffusion) could decrease Fe densities near the layer peak by up to a third [*Feng et al.*, 2013]. However, there are limits on adjusting the Prandtl number, since it also is used in the calculation of diffusion of heat and other trace species. Also, drastically increasing the loss rate will diminish the importance of transport, as discussed above, and reduce the magnitude of the high-latitude seasonal cycle. If the dimerization rate coefficient is increased to make irreversible chemical loss faster, it would also have the effect of depleting Na on the bottom side of the layer, effectively pushing up the peak of the layer to above the observed peak altitude around 90 km. Thus, although the MIF includes our current astronomical understanding of the sporadic meteor complex, future and more accurate versions of WACCM with Na chemistry will set further constraints to the mass input of extraterrestrial material.

[30] In the paper by *Feng et al.* [2013], we describe the inclusion of mesospheric Fe chemistry into WACCM. In order to achieve satisfactory agreement with lidar observations of the Fe layer, the MIF used in the present paper had to be reduced by a factor of just over 2, corresponding to a total meteoric mass input of 2.1 t d^{-1}. A similar reduction in the injection rate of Fe compared with Na has also been noted in a one-dimensional model study of these layers at the South Pole [*Gardner et al.*, 2005]. The implication of this may be that the meteor velocity distribution used to calculate the MIF should be shifted to lower velocities, when differential ablation between a volatile element such as Na and a more refractory one like Fe becomes more pronounced [*Vondrak et al.*, 2008]. Alternatively, an additional chemical sink for Fe may be present in the MLT. However, this is less likely to be the case since the height of the Fe layer is correctly modeled to be around 85 km, about 5 km lower than the Na peak.

[31] In summary, this paper has presented the first global model of meteoric Na that combines a chemistry-climate model with a meteoroid input function that specifies the temporal and geographical input of meteoric Na into the upper atmosphere. The model predictions are in good agreement with a Na reference atmosphere derived from a combination of Odin and ground-based observations. This agreement is achieved with a relatively low input of atomic Na equivalent to a total meteoric ablated mass of 4.6 t d^{-1}. Our simulations and new climatology confirm the finding of *Fussen et al.* [2010] of a shift from semiannual to annual variation in the Na column with increasing latitude. Analysis of Na species chemical production, loss, and transport shows that the high-latitude annual cycle in Na, which peaks in wintertime, is driven by the mean meridional circulation. When this circulation is drastically perturbed, such as during a major stratospheric sudden warming, very large changes in the Na column are simulated. Our study illustrates that due to larger sensitivity of mesospheric sodium to dynamics, reproducing its observed variability provides a stringent test of global models and should help to constrain key atmospheric variables in this poorly sampled region of the atmosphere.

[32] **Acknowledgments.** The National Center for Atmospheric Research is operated by the University Corporation for Atmospheric Research under sponsorship of the National Science Foundation. The MIF was developed under NSF Grants ATM-05311464, ATM-0525655, ATM-0634650, and AST-0908118 to NorthWest Research Associates. We also acknowledge support by the UK Natural Environment Research Council (NERC grant NE/G019487/1).

References

Bardeen, C. G., O. B. Toon, E. J. Jensen, D. R. Marsh, and V. L. Harvey (2008), Numerical simulations of the three-dimensional distribution of meteoric dust in the mesosphere and upper stratosphere, *J. Geophys. Res.*, *113*, D17202, doi:10.1029/2007JD009515.

Bilitza, D. (2003), International reference ionosphere 2000: Examples of improvements and new features, *Adv. Space Res.*, *31*(3), 757–767.

Butler, A. H., and L. M. Polvani (2011), El Niño, La Niña, and stratospheric sudden warmings: A reevaluation in light of the observational record, *Geophys. Res. Lett.*, *38*, L13807, doi:10.1029/2011GL048084.

Calvo, N., R. R. Garcia, D. R. Marsh, M. J. Mills, D. E. Kinnison, and P. J. Young (2012), Reconciling modeled and observed temperature trends over Antarctica, *Geophys. Res. Lett.*, *39*, L16803, doi:10.1029/2012GL052526.

Ceplecha, Z., J. Borovička, W. Elford, D. Revelle, R. Hawkes, V. Porubčan, and M. Šimek (1998), Meteor phenomena and bodies, *Space Sci. Rev.*, *84*, 327–471.

Clemesha, B. R., D. M. Simonich, P. P. Batista, T. Vondrak, and J. M. C. Plane (2004), Negligible long-term temperature trend in the upper atmosphere at 23°S, *J. Geophys. Res.*, *109*, D05302, doi:10.1029/2003JD004243.

Clemesha, B. R., D. M. Simonich, P. P. Batista, and V. W. J. H. Kirchhoff (1982), The diurnal variation of atmospheric sodium, *J. Geophys. Res.*, *87*(A1), 181–186, doi:10.1029/JA087iA01p00181.

Fan, Z. Y., J. M. C. Plane, J. Gumbel, J. Stegman, and E. J. Llewellyn (2007), Satellite measurements of the global mesospheric sodium layer, *Atmos. Chem. Phys.*, *7*(15), 4107–4115, doi:10.5194/acp-7-4107-2007.

Feng, W., D. R. Marsh, M. P. Chipperfield, D. Janches, D. Höffner, F. Yi, and J. M. C. Plane (2013), A global atmospheric model of meteoric iron, *J. Geophys. Res. Atmos.*, *118*, 9456–9474, doi:10.1002/jgrd.50708.

Fentzke, J. T., and D. Janches (2008), A semi-empirical model of the contribution from sporadic meteoroid sources on the meteor input function in the MLT observed at Arecibo, *J. Geophys. Res.*, *113*, A03304, doi:10.1029/2007JA012531.

Fentzke, J. T., D. Janches, I. Strelnikova, and M. Rapp (2009), Meteoric smoke particle properties derived using dual-beam Arecibo UHF observations of *D*-region spectra during different seasons, *J. Atmos. Sol. Terr. Phys.*, *71*(17-18), 1982–1991, doi:10.1016/j.jastp.2009.09.002.

Fussen, D., et al. (2010), A global climatology of the mesospheric sodium layer from GOMOS data during the 2002–2008 period, *Atmos. Chem. Phys.*, *10*, 9225–9236, doi:10.5194/acp-10-9225-2010.

Gardner, C. S., J. M. C. Plane, W. Pan, T. Vondra, B. J. Murray, and X. Chu (2005), Seasonal variations of the Na and Fe layers at the South Pole and their implications for the chemistry and general circulation of the polar mesosphere, *J. Geophys. Res.*, *110*, D10302, doi:10.1029/2004JD005670.

Gumbel, J., Z. Y. Fan, T. Waldemarsson, J. Stegman, G. Witt, E. J. Llewellyn, C.-Y. She, and J. M. C. Plane (2007), Retrieval of global mesospheric sodium densities from the Odin satellite, *Geophys. Res. Lett.*, *34*, L04813, doi:10.1029/2006GL028687.

Jackman, C. H., D. R. Marsh, F. M. Vitt, R. R. Garcia, C. E. Randall, E. L. Fleming, and S. M. Frith (2009), Long-term middle atmospheric influence of very large solar proton events, *J. Geophys. Res.*, *114*, D11304, doi:10.1029/2008JD011415.

Janches, D., C. J. Heinselman, J. L. Chau, A. Chandran, and R. Woodman (2006), Modeling the global micrometeor input function in the upper atmosphere observed by high power and large aperture radars, *J. Geophys. Res.*, *111*, A07317, doi:10.1029/2006JA011628.

Janches, D., S. Close, and J. T. Fentzke (2008), A comparison of detection sensitivity between ALTAIR and Arecibo meteor observations: Can high power and large aperture radars detect low velocity meteor head-echoes, *Icarus*, *193*(1), 105–111, doi:10.1016/j.icarus.2007.08.022.

Janches, D., L. P. Dyrud, S. L. Broadley, and J. M. C. Plane (2009), First observation of micrometeoroid differential ablation in the atmosphere, *Geophys. Res. Lett.*, *36*, L06101, doi:10.1029/2009GL037389.

Kinnison, D. E., et al. (2007), Sensitivity of chemical tracers to meteorological parameters in the MOZART-3 chemical transport model, *J. Geophys. Res.*, *112*, D20302, doi:10.1029/2006JD007879.

Kopp, E. (1997), On the abundance of metal ions in the lower ionosphere, *J. Geophys. Res.*, *102*(A5), 9667–9674, doi:10.1029/97JA00384.

Kopp, G., and J. L. Lean (2011), A new, lower value of total solar irradiance: Evidence and climate significance, *Geophys. Res. Lett.*, *38*, L01706, doi:10.1029/2010GL045777.

Lean, J., G. Rottman, J. Harder, and G. Kopp (2005), SORCE contributions to new understanding of global change and solar variability, *Sol. Phys.*, *230*, 27–53, doi:10.1007/s11207-005-1527-2.

Marsh, D. R. (2011), Chemical-dynamical coupling in the mesosphere and lower thermosphere, in *Aeronomy of the Earth's Atmosphere and Ionosphere,* vol. 2, edited by M. Ali Abdu and D. Pancheva, pp. 3–17, Springer, Netherlands, doi:10.1007/978-94-007-0326-1.

Marsh, D. R., R. R. Garcia, D. E. Kinnison, B. A. Boville, F. Sassi, S. C. Solomon, and K. Matthes (2007), Modeling the whole atmosphere response to solar cycle changes in radiative and geomagnetic forcing, *J. Geophys. Res.*, *112*, D23306, doi:10.1029/2006JD008306.

Marsh, D. R., M. Mills, D. Kinnison, J.-F. Lamarque, N. Calvo, and L. Polvani (2013), Climate change from 1850 to 2005 simulated in CESM1(WACCM), *J. Clim.*, *26*(19), 7372–7391, doi:10.1175/JCLI-D-12-00558.

Neale, R., J. Richter, S. Park, P. Lauritzen, S. Vavrus, P. Rasch, and M. Zhang (2013), The mean climate of the Community Atmosphere Model (CAM4) in forced SST and fully coupled experiments, *J. Clim.*, *26*(14), 5150–5168, doi:10.1175/JCLI-D-12-00236.1.

Pifko, S., D. Janches, S. Close, J. J. Sparks, T. Nakamura, and D. Nesvorný (2013), The meteoroid input function and predictions of mid-latitude meteor observations by the MU radar, *Icarus*, *223*, 444–459, doi:10.1016/j.icarus.2012.12.014.

Plane, J. M. C. (2000), The role of sodium bicarbonate in the nucleation of noctilucent clouds, *Ann. Geophys.*, *18*(7), 807–814, doi:10.1007/s00585-000-0807-2.

Plane, J. M. C. (2004), A time-resolved model of the mesospheric Na layer: Constraints on the meteor input function, *Atmos. Chem. Phys.*, *4*(3), 627–638, doi:10.5194/acp-4-627-2004.

Plane, J. M. C. (2012), Cosmic dust in the Earth's atmosphere, *Chem. Soc. Rev.*, *41*, 6507–6518, doi:10.1039/C2CS35132C.

Plane, J. M. C., C. S. Gardner, J. Yu, C. Y. She, R. R. Garcia, and H. C. Pumphrey (1999), Mesospheric Na layer at 40°N: Modeling and observations, *J. Geophys. Res.*, *104*(D3), 3773–3788, doi:10.1029/1998JD100015.

Plane, J. M. C., B. J. Murray, X. Chu, and C. S. Gardner (2004), Removal of meteoric iron on polar mesospheric clouds, *Science*, *304*, 426–428.

Rienecker, M. M., et al. (2011), MERRA: NASA's Modern-Era Retrospective Analysis for Research and Applications, *J. Clim.*, *24*(14), 3624–3648, doi:10.1175/JCLI-D-11-00015.1.

She, C. Y., S. Chen, Z. Hu, J. Sherman, J. D. Vance, V. Vasoli, M. A. White, J. Yu, and D. A. Krueger (2000), Eight-year climatology of nocturnal temperature and sodium density in the mesopause region (80 to 105 km) over Fort Collins, CO (41°N, 105°W), *Geophys. Res. Lett.*, *27*(20), 3289–3292, doi:10.1029/2000GL003825.

Smith, A. K. (2012), Global dynamics of the MLT, *Surv. Geophys.*, *33*, 1177–1230, doi:10.1007/s10712-012-9196-9.

Smith, A. K., R. R. Garcia, D. R. Marsh, and J. H. Richter (2011), WACCM simulations of the mean circulation and trace species transport in the winter mesosphere, *J. Geophys. Res.*, *116*, D20115, doi:10.1029/2011JD016083.

States, R. J., and C. S. Gardner (1999), Structure of the mesospheric Na layer at 40°N latitude: Seasonal and diurnal variations, *J. Geophys. Res.*, *104*(D9), 11,783–11,798, doi:10.1029/1999JD900002.

Tilgner, C., and U. von Zahn (1988), Average properties of the sodium density distribution as observed at 69°N latitude in winter, *J. Geophys. Res.*, *93*(D7), 8439–8454, doi:10.1029/JD093iD07p08439.

Vondrak, T., J. M. C. Plane, S. Broadley, and D. Janches (2008), A chemical model of meteoric ablation, *Atmos. Chem. Phys.*, *8*(23), 7015–7031, doi:10.5194/acp-8-7015-2008.

Xu, J., and A. K. Smith (2003), Perturbations of the sodium layer: Controlled by chemistry or dynamics?, *Geophys. Res. Lett.*, *30*(20), 2056, doi:10.1029/2003GL018040.

Xu, J., and A. K. Smith (2004), Studies of gravity wave-induced fluctuations of the sodium layer using linear and nonlinear models, *J. Geophys. Res.*, *109*, D02306, doi:10.1029/2003JD004038.

Xu, J., A. K. Smith, R. L. Collins, and C.-Y. She (2006), Signature of an overturning gravity wave in the mesospheric sodium layer: Comparison of a nonlinear photochemical-dynamical model and lidar observations, *J. Geophys. Res.*, *111*, D17301, doi:10.1029/2005JD006749.

Yi, F., C. Yu, S. Zhang, X. Yue, X. He, C. Huang, Y. Zhang, and K. Huang (2009), Seasonal variations of the nocturnal mesospheric Na and Fe layers at 30°N, *J. Geophys. Res.*, *114*, D01301, doi:10.1029/2008JD010344.

Yuan, T., B. Thurairajah, C.-Y. She, A. Chandran, R. L. Collins, and D. A. Krueger (2012), Wind and temperature response of midlatitude mesopause region to the 2009 sudden stratospheric warming, *J. Geophys. Res.*, *117*, D09114, doi:10.1029/2011JD017142.

Zhou, Q., J. Friedman, S. Raizada, C. Tepley, and Y. T. Morton (2005), Morphology of nighttime ion, potassium and sodium layers in the meteor zone above Arecibo, *J. Atmos. Sol. Terr. Phys.*, *67*(13), 1245–1257, doi:10.1016/j.jastp.2005.06.013.